Understanding structural distortions in hybrid layered perovskites with the n = 1 Ruddlesden-Popper structure

Authors

Tianyu Liu[a], Noah P. Holzapfel[a] and Patrick M. Woodward[a]*

[a]Department of Chemistry and Biochemistry, The Ohio State University, 100 West 18th Avenue, Columbus, Ohio, 43210, United States

Correspondence email: woodward.55@osu.edu

Funding information National Science Foundation, Directorate for Mathematical and Physical Sciences (grant No. 2003793).

Synopsis Structural distortions in hybrid organic-inorganic layered halide perovskites with the Ruddlesden-Popper structure are classified into 47 different patterns of octahedral tilting via symmetry mode analysis. A survey of known compounds shows that tilt systems with both out-of-phase ϕ-tilts about the *a*- and/or *b*-axes and θ-tilts about the *c*-axis are favored over other patterns of octahedral tilting because this combination leads to favorable hydrogen bonding interactions between the organic cations and the inorganic layers.

Abstract A symmetry mode analysis yields 47 symmetrically distinct patterns of octahedral tilting in hybrid organic-inorganic layered perovskites that adopt the $n = 1$ Ruddlesden-Popper structure. The crystal structures of compounds belonging to this family are compared to the predictions of the symmetry analysis. Approximately 88% of the 140 unique structures have symmetries that agree with those expected based on octahedral tilting alone, while the remaining compounds have additional structural features that further lower the symmetry, such as asymmetric packing of bulky organic cations, distortions of metal-centered octahedra, or a shift of the inorganic layers that deviates from the $a/2 + b/2$ shift associated with the Ruddlesden-Popper structure. The structures of real compounds are heterogeneously distributed amongst the various tilt systems, with only 9 of the 47 tilt systems represented. No examples of in-phase ψ-tilts about the *a*- and/or *b*-axes of the undistorted parent structure were found, while at the other extreme ~66% of the known structures possess a combination of out-of-phase ϕ-tilts about the *a*- and/or *b*-axes and θ-tilts (rotations) about the *c*-axis. The latter combination leads to favorable hydrogen bonding interactions that accommodate the chemically inequivalent halide ions within the inorganic layers. In some compounds, primarily those that contain

either Pb^{2+} or Sn^{2+}, favorable hydrogen bonding interactions can also be achieved by distortions of the octahedra in combination with θ-tilts.

Keywords: perovskites; symmetry mode analysis; organic-inorganic hybrid materials; Ruddlesden-Popper structure

1. Introduction

The past decade has seen a resurgence in the study of hybrid halide perovskites, driven in part by the demonstration that high efficiency, solution processable photovoltaic cells can be made from materials like $(CH_3NH_3)PbI_3$ (Stranks, *et al*. 2013; Baike, *et al*., 2014; Frost, *et al*. 2014). The intense and sustained study of this family of materials has led to the discovery of many properties that are of interest for applications. Examples include photoluminescence (Stompous, *et al*. 2018; Majher, *et al*. 2019; Gray, *et al*. 2019), electroluminescence (Lin, *et al*. 2018), ferroelectricity (Liao, *et al*. 2015), low dimensional magnetism (Asensio, et al. 2022), and colossal barocaloric effects (Li, et al. 2021; Seo, *et al*. 2022) among others.

Compositions with the three-dimensional (3D) perovskite framework are limited to those containing relatively small organic cations, like methylammonium and formamidinium. This restriction is lifted in two-dimensional (2D) layered perovskites where the octahedral connectivity in one direction is broken, leading to a vast family of hybrid layered perovskites. Broadly speaking these can be further categorized into two groups. Those that fall into the Dion-Jacobson (DJ) family, where the inorganic layers stack in such a way that the octahedra line up on top of one another when viewed perpendicular to the layers (Figure 1a), and those that fall into the Ruddlesden-Popper (RP) family, where the layers are offset by $a/2 + b/2$, so that the octahedra in each layer sit over the cavities in the adjacent layers (Figure 1b). Amongst all-inorganic compositions with layers one octahedron thick, RP phases have twice as many large "A-site" cations as octahedra, giving a stoichiometry of A_2BX_4, whereas the DJ phases have a stoichiometry of ABX_4. However, in hybrid phases, the patterns of layer stacking are such that it is not always possible to classify compounds as belonging to the DJ or RP families from their composition alone. The structural implications of layer stacking patterns, including layer shifts intermediate between the DJ and RP phases, are discussed at length in a recent paper by McNulty and Lightfoot (2021).

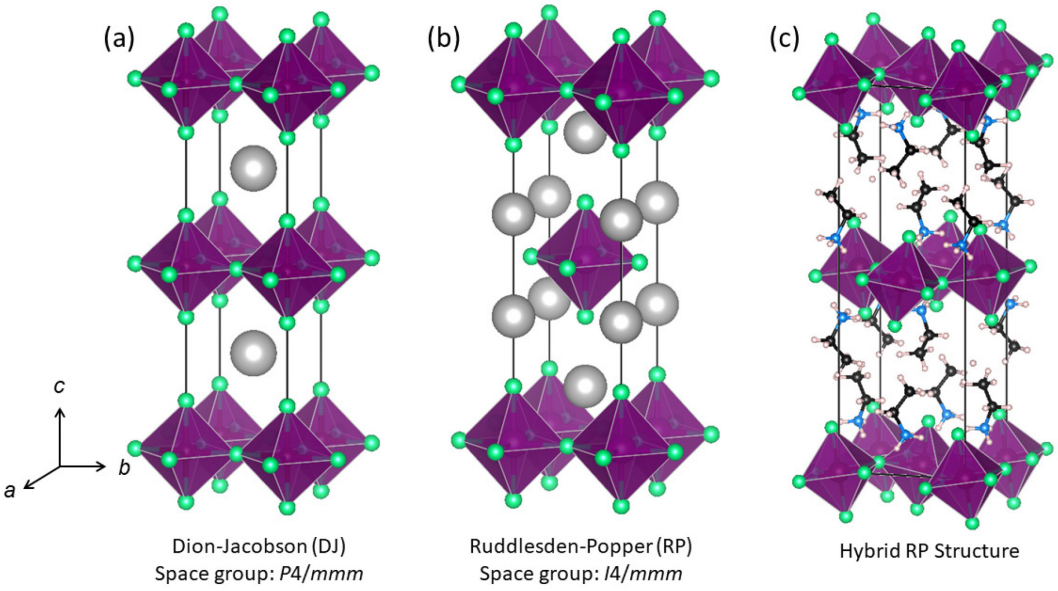

Figure 1: (a) The undistorted n = 1 Dion-Jacobson (DJ) structure type. (b) The undistorted n = 1 Ruddlesden-Popper (RP) structure type. (c) A hybrid layered perovskite with the n = 1 RP structure that exhibits octahedral tilting. For the DJ structure, two unit cells in the c-direction are shown for ease of comparison.

The prevalence of rotations or tilts of essentially rigid octahedra among 3D perovskites has long been appreciated (Glazer, 1972; Woodward, 1997a; Woodward, 1997b; Stokes & Howard, 1998; Stokes, et al. 2002; Howard, et al. 2003). Octahedral tilting distortions can have a dramatic impact on the physical properties of 3D inorganic perovskites and these distortions are often used to fine tune the properties of both oxide and halide perovskites (Hwang, et al. 1995; Mahesh, et al. 1995; Attfield 1998; Linaberg, *et al*. 2017). By and large, this approach to materials design has not been widely applied to hybrid layered perovskites (Figure 1c), even though octahedral tilting distortions appear to be ubiquitous amongst these compounds (McNulty & Lightfoot, 2021). Nevertheless, there is every reason to believe that the optical, electrical, and magnetic properties of hybrid layered perovskites can be tuned through the control of octahedral tilting distortions in a manner similar to that used for 3D oxide perovskites. To rationally design materials optimized for applications it is critical to understand the forces that drive octahedral tilting distortions. A detailed understanding of the crystal chemistry becomes even more important for phenomena that only emerge for specific structural distortions, like ferroelectricity.

In the first part of this paper, symmetry mode analysis is used to determine the space groups and unit cells associated with various patterns of octahedral tilting. To retain a manageable scope, the analysis

is limited to RP phases with inorganic layers a single octahedron thick (n = 1 RP phases). The results for tilts/rotations perpendicular to the layers (θ-tilts) and/or out-of-phase tilts within the layers (ϕ-tilts) largely agree with the earlier analysis of Hatch, et al. (1989), although some important differences are noted. Next, the analysis is extended to encompass in-phase tilts within the layers (ψ-tilts), which have not previously been considered. The results of the symmetry mode analysis are then compared to a tabulation of the crystal structures of known hybrid n = 1 RP phases. This comparison is used to determine the extent to which octahedral tilting distortions alone can be used to predict the symmetries of distorted structures, and to determine the patterns of octahedral tilting that are most common. Finally, hydrogen bonding interactions between the organic cations and inorganic layers are examined to better understand how they drive octahedral tilting distortions in hybrid layered perovskites. By going beyond classification and focusing on the crystal chemistry that drives these distortions it is hoped that this study will advance the ability of scientists to rationally design hybrid layered perovskites with useful physical properties.

2. Notation for describing octahedral tilting in *n* = 1 RP phases

There are two notations for describing octahedral tilting in perovskites, one developed by Glazer (1972) and the other by Alexandrov (1987). Glazer's notation is widely used for three dimensional perovskites, but it has some limitations when applied to layered perovskites with the Ruddlesden-Popper structure. Because the undistorted parent structure is tetragonal ($I4/mmm$) rather than cubic ($Pm\bar{3}m$), the symmetry consequences of tilting about the c-axis are different than tilting about the a- and b-axes. More importantly, the offset of $a/2 + b/2$ from one layer to the next means that the octahedra in adjacent layers are not aligned on top of one another and therefore one cannot speak of in-phase or out-of-phase tilting about the c-axis, at least not for n = 1 Ruddlesden-Popper phases. For these reasons the notation developed by Alexandrov is used throughout this paper.

Figure 2a shows an undistorted inorganic layer from a hybrid n = 1 Ruddlesden-Popper phase. Rotations of the octahedra about the c-axis of the tetragonal parent structure are denoted by the Greek letter θ and are illustrated in Figure 2b. Rotations about the a- and/or b-axes can be either in-phase or out-of-phase and are represented by the Greek letters ψ and ϕ, respectively. Figure 2c illustrates in-phase ψ-tilts around the b-axis, denoted as (0ψ0). Simultaneous ψ tilts around both a and b are also possible, as illustrated by the (ψψ0) tilt system in Figure 2d. If there are tilts about two axes, but of different magnitudes, subscripts are used to signify their inequivalence ($\psi_1\psi_2$0). The same convention is used to describe out-of-phase ϕ-tilts. Examples of layers with (0ϕ0) and (ϕϕ0) tilting are illustrated in Figures 2e and 2f, respectively.

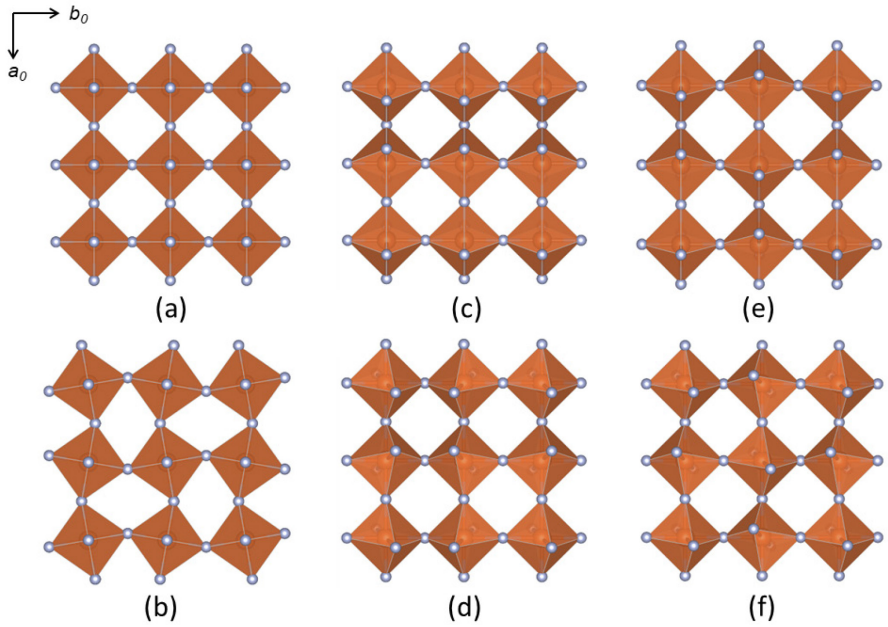

Figure 2: Types of octahedral tilting in layers of linked octahedra: (a) no tilting; (b) (00θ); (c) (0ψ0), (d) (ψψ0), (e) (0ϕ0), and (f) (ϕϕ0).

Because the octahedra in different layers are not connected, the tilting pattern in a given layer is in principle independent of the tilting in neighboring layers. To account for this, the tilting in each layer must be specified, for example, (ϕ00) tilting in layer 1 and (ϕϕθ) tilting in layer 2 would be written (ϕ00)/(ϕϕθ). More complicated schemes where more than two layers are needed to capture the periodicity of the tilts are rare and therefore not considered in this analysis. In practice, the tilts are generally the same from one layer to the next, however, the directions of the tilts can differ from layer to layer, and this can have symmetry consequences, as discussed below.

To compare the direction of tilting in alternating layers, we compare the octahedron at the origin of the parent *I*4/*mmm* cell in one layer to the octahedron at the body center in the next layer. If these two octahedra tilt in the opposite direction it is written as either $\bar{\theta}$, $\bar{\psi}$ or $\bar{\phi}$. In some cases, changing the direction of a tilt in layer 2 may not lead to a distinct tilt system. However, there are examples, such as (ϕϕθ)/(ϕϕθ) and (ϕϕθ)/(ϕϕ$\bar{\theta}$), where changing the direction of one or more rotations in the second layer (but keeping the magnitude the same) does lead to a structure with symmetry that is distinct from other tilt systems.

3. Symmetry Mode Analysis

Aleksandrov and co-workers originally confronted the problem of octahedral tilting in the A_2BX_4 crystal structure through a direct crystallographic approach (Aleksandrov, 1987; Aleksandrov, et al., 1987a). Their method consisted of physically depicting the movement of atoms caused by different

variations of tilting and using this depiction to determine the symmetry elements present. Once the symmetry elements had been identified a space group assignment could be made. Hatch et al. (1989) implemented a more systematic method for obtaining subgroups resulting from a single distortion. This analysis was carried out using a computational program that incorporated Landau's theory of continuous phase transitions. Campbell, et al. (2006) have further developed this computer program into the ISODISTORT software suite, which can be used to explore the structural distortion modes of crystalline materials from a parent structure type. Here we use ISODISTORT to revisit the earlier analysis and expand it to include in-phase ψ tilts.

To determine the effects of various types of octahedral tilting on the $n = 1$ Ruddlesden-Popper structure we use the crystal structure of K_2NiF_4 as the archetype or parent structure (Yeh, *et al*., 1993). This structure has tetragonal *I*4/*mmm* space group symmetry and unit cell parameters of $a_0 \times a_0 \times c_0$ (Figure 1b). The subgroups determined by ISODISTORT were visualized with the ISOVIZ application which allowed the respective tilting scheme to be identified by visual inspection. The symmetry analysis was limited to structural distortion modes that can be described as rotations of the Ni-centered octahedra. Note that because hybrid layered perovskites with the DJ structure have a different parent structure, one with *P*4/*mmm* space group symmetry, the results of our analysis do not apply to DJ compounds or to compounds with layer shifts intermediate between RP and DJ phases. Interested readers are directed to earlier works by Aleksandrov, et al. (1987b), Aleksandrov and Bartolome (2001), and McNulty & Lightfoot (2021) for a symmetry analysis of layered perovskites with the DJ structure. It should also be noted that the symmetry consequences of octahedral tilting in $A_{n+1}B_nX_{3n+1}$ RP phases differ depending on whether n is even or odd (Aleksandrov & Bartolome, 1994).

Hatch, et al. (1989) previously identified the following irreducible representations (irreps) as being associated with the tilting of rigid octahedra: X_2^+, X_3^+, X_4^+, N_1^+, P_4, and P_5. The symbols follow the notation of Miller & Love (1967), where the first term denotes the k-point of the Brillouin zone of the parent cell, and the superscript tells whether the inversion center at the origin is retained (+) or lost (−). The distortions associated with the N and P irreps correspond to complex patterns of octahedral tilting that require more than two layers before repeating. As these types of octahedral tilting are rarely encountered, they are not investigated further here. Readers interested in those patterns of octahedral tilting should revisit the original work (Hatch, et al., 1989). It should also be noted that none of the six irreps listed above corresponds to in-phase ψ tilts. To expand the analysis to include ψ tilts, the incommensurate k-point, SM (a,0,0), must be included as one arm of the X k-point with $a = ½$.

Four irreps are found to be responsible for the tilts discussed in the previous section: X_2^+ induces θ tilts, X_3^+ and X_4^+ induce ϕ tilts, and SM3 induces ψ tilts. Note that these irreps are labeled with respect to the *I*4/*mmm* parent cell of the Ruddlesden-Popper structure, with the octahedral cation at the origin.

Examples of each are shown in the Supporting Information (Figure S1). The θ tilts can be described as rotations about the 4-fold axes that run parallel to the *c*-axis of the parent cell. The ψ tilts are in-phase rotations about axes that run parallel to either the *a*- or *b*-axis of the parent cell, and the ϕ tilts are out-of-phase rotations about axes that run along the face diagonals of the parent cell, either [110] or [$\bar{1}$10]. Though X_3^+ and X_4^+ are both responsible for ϕ tilts, they lead to different tilts from one layer to the next, as shown in Figure 3. If there is a clockwise tilt about [110] in layer 1 the X_3^+ irrep will produce a clockwise tilt about the same axis in layer 2, whereas the X_4^+ irrep will produce a counterclockwise tilt about this axis in layer 2.

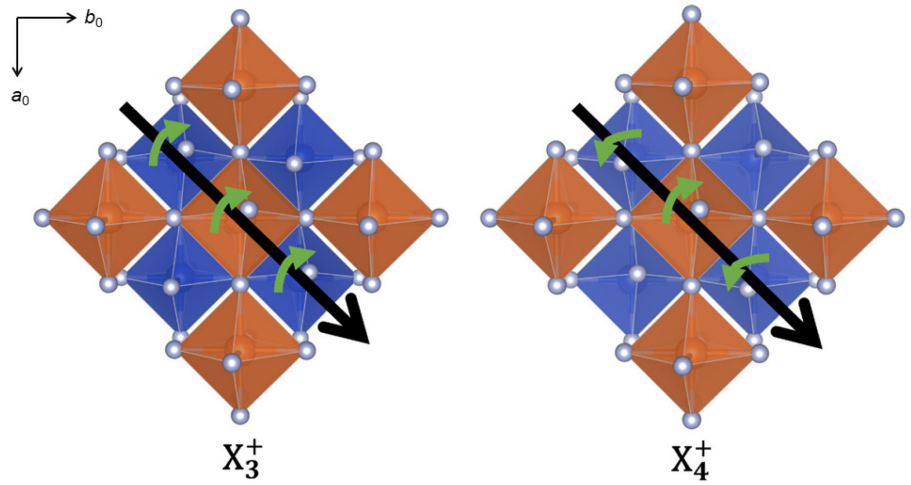

Figure 3: A top-down view of two distorted variants of the K_2NiF_4 structure showing the differences between X_3^+ and X_4^+ irreps that correspond to order parameter (0, a). For clarity, the octahedra in the upper layer are depicted as orange octahedra, and those in the lower layer in blue. The X_3^+ irrep leads to ϕ tilts around an axis parallel to [110] that have the same sense in all layers (left). The X_4^+ irrep produces the same ϕ tilts in the upper layer, but the direction of those tilts is reversed in adjacent layers (right).

Within the framework of Landau theory, the magnitude of each distortion is represented by an order parameter *g*. The order parameter identifies the invariant subspace containing all distortion vectors that possess the related distortion symmetry. Since the X_2^+, X_3^+, and X_4^+ irreps are all two dimensional, two order parameters (g_1 and g_2) are associated with each irrep. For X_2^+ one order parameter signifies the magnitude of the rotation about the 4-fold axis in layers 1 and 2 (the *c*-axis of the parent cell). When the order parameter is (0, a) the octahedra in layers 1 and 2 rotate by the same magnitude, but the octahedron at the origin and the one at the body center rotate in the opposite sense so that the tilt system is (00θ)/(00$\bar{\theta}$). The second order parameter also describes rotations about the 4-fold axis, but the directions of the rotations alternate between adding to and opposing the rotations associated with

the first order parameter. Hence, when the X_2^+ order parameter is (a, a) the rotations cancel in one layer and add in the second layer, giving the tilt system (000)/(00θ). When the magnitudes of the two order parameters are different, (a, b) they produce rotations of different magnitudes in layers 1 and 2, giving the tilt system $(00\theta_1)/(00\theta_2)$. From a symmetry perspective the tilt system (00θ)/(00θ) is a special case of $(00\theta_1)/(00\theta_2)$. In this structure, which has orthorhombic *Pbam* symmetry, there is no symmetry element that forces the rotations in one layer to be equal to those in the layers above and below. This result differs from the earlier work of Hatch et al. (1989) where the symmetry associated with (00θ)/(00θ) tilting was erroneously listed as being identical to $(00\theta)/(00\bar{\theta})$.

As mentioned previously, the X_3^+ and X_4^+ irreps are associated with ϕ tilts and correspond to rotations about face diagonals of the parent unit cell. When the order parameter is (0, a) the tilts are about [110] in each layer. For X_3^+ when the order parameter is (0, a) this leads to the (ϕϕ0)/(ϕϕ0) tilt system, while for the X_4^+ irrep the tilt system is $(\phi\phi0)/(\bar{\phi}\bar{\phi}0)$. These two patterns of octahedral tilting are illustrated in Figure 3. The order parameter (a, a) represents tilts about axes that run along both the [110] or $[\bar{1}10]$. The net effect of this combination is a tilt about [100] in the first layer and [010] in the second layer, leading to the tilt system (ϕ00)/(0ϕ0) for X_3^+ and $(\phi00)/(0\bar{\phi}0)$ for X_4^+. If the order parameter is (a, b) the tilt systems that result are $(\phi_1\phi_2 0)/(\phi_2\phi_1 0)$ and $(\phi_1\phi_2 0)/(\bar{\phi}_2\bar{\phi}_1 0)$ for X_3^+ and X_4^+, respectively.

The results of our analysis for θ tilts, ϕ tilts, and combinations of the two are given in Table 1. In addition to the nine tilt systems associated with a single irrep and described above, an additional sixteen tilt systems arise from the coupling of multiple irreps. The results of this analysis are in reasonably good agreement with the previous work of Hatch, et al. (1989), but there are some differences. In addition to the differences in the tilt systems involving only θ-tilts discussed above, we obtain 25 unique tilt systems, an increase of three from the 22 that were previously reported. The additional tilt systems involve either coupling of X_3^+ and X_4^+ irreps or coupling of all three irreps. We also find that the tilt system previously reported as $(\phi_1\phi_2\theta)/(\bar{\phi}_2\phi_1\theta)$ should be classified as $(\phi_1\phi_2\theta)/(\bar{\phi}_2\bar{\phi}_1\theta)$, as shown in the Supporting Information (Figure S2).

Table 1: Space group assignments and tilting schemes that arise from the combination of θ and/or ϕ tilts for n = 1 Ruddlesden-Popper phases.

#	Tilts		Space group	X_3^+	X_4^+	X_2^+	Basis	Origin
	1st layer	2nd layer						
1	00θ	00$\bar{\theta}$	*Cmce*	(0, 0)	(0, 0)	(0, a)	(0,0,1), (1,1,0), ($\bar{1}$,1,0)	(0,0,0)
2	000	00θ	*P*4/*mbm*	(0, 0)	(0, 0)	(a, a)	(1,1,0), ($\bar{1}$,1,0), (0,0,1)	(½,½,0)
3	00θ_1	00θ_2	*Pbam*	(0, 0)	(0, 0)	(a, b)	(1,1,0), ($\bar{1}$,1,0), (0,0,1)	(0,0,0)
4	ϕϕ0	ϕϕ0	*Cmce*	(0, a)	(0, 0)	(0, 0)	(1,1,0), (0,0,1), (1, $\bar{1}$,0)	(0,0,0)
5	ϕ00	0ϕ0	*P*4$_2$/*ncm*	(a, a)	(0, 0)	(0, 0)	(1,1,0), ($\bar{1}$,1,0), (0,0,1)	(0,0,0)
6	$\phi_1\phi_2$0	$\phi_2\phi_1$0	*Pccn*	(a, b)	(0, 0)	(0, 0)	(1,1,0), ($\bar{1}$,1,0), (0,0,1)	(0,0,0)
7	ϕϕ0	$\bar{\phi}\bar{\phi}$0	*Cccm*	(0, 0)	(a, 0)	(0, 0)	(0,0,1), (1, $\bar{1}$,0), (1,1,0)	(−¼,¼,¼)
8	ϕ00	0$\bar{\phi}$0	*P*4$_2$/*nnm*	(0, 0)	(a, a)	(0, 0)	(1,1,0), ($\bar{1}$,1,0), (0,0,1)	(½,½,0)
9	$\phi_1\phi_2$0	$\bar{\phi}_2\bar{\phi}_1$0	*Pnnn*	(0, 0)	(a, b)	(0, 0)	(1,1,0), ($\bar{1}$,1,0), (0,0,1)	(0,0,0)
10	ϕϕθ	ϕϕθ	*Pbca*	(0, a)	(0, 0)	(b, 0)	(0,0,1), (1, $\bar{1}$,0), (1,1,0)	(0,0,0)
11	ϕϕθ	ϕϕ$\bar{\theta}$	*P*2$_1$/*c*	(0, a)	(0, 0)	(0, b)	(½,½,½), ($\bar{1}$,1,0), ($\bar{1}$, $\bar{1}$,0)	(0,0,0)
12	$\phi_1\phi_2\theta$	$\phi_2\phi_1\bar{\theta}$	*P*2$_1$/*c*	(a, b)	(0, 0)	(0, c)	(1,1,0), ($\bar{1}$,1,0), (0,0,1)	(0,0,0)
13	ϕϕθ	$\bar{\phi}\bar{\phi}\theta$	*Pccn*	(0, 0)	(a, 0)	(b, 0)	(0,0,1), ($\bar{1}$, $\bar{1}$,0), (1, $\bar{1}$,0)	(0,0,0)
14	ϕϕθ	$\bar{\phi}\bar{\phi}\bar{\theta}$	*C*2/*c*	(0, 0)	(a, 0)	(0, b)	(0,0, $\bar{1}$), ($\bar{1}$,1,0), (1,1,0)	(¼,−¼,−¼)
15	$\phi_1\phi_2\theta$	$\bar{\phi}_2\bar{\phi}_1\bar{\theta}$	*P*2/*c*	(0, 0)	(a, b)	(0, c)	(1, $\bar{1}$,0), (1,1,0), ($\bar{1}$,1,1)	(0,0,0)
16	$\phi_1\phi_2$0	$\phi_1\phi_2$0	*C*2/*c*	(0, a)	(0, b)	(0, 0)	(1,1,0), (0,0, $\bar{1}$), ($\bar{1}$,1,0)	(¼,¼,−¼)
17	$\phi_1\phi_1$0	$\phi_2\phi_2$0	*Pmna*	(0, a)	(b, 0)	(0, 0)	(1,1,0), (0,0,1), (1, $\bar{1}$,0)	(0,0,0)
18	$\phi_1$00	0$\phi_2$0	*Cmma*	(a, a)	(b, b)	(0, 0)	(2,0,0), (0, $\bar{2}$,0), (0,0, $\bar{1}$)	(0,0,0)
19	$\phi_1\phi_2$0	$\bar{\phi}_2\phi_1$0	*P*4$_2$/*n*	(a, a)	(b,−b)	(0, 0)	(1,1,0), ($\bar{1}$,1,0), (0,0,1)	(½,−½,−½)
20	$\phi_1\phi_2$0	$\phi_3\phi_4$0	*P*2/*c*	(a, b)	(c, d)	(0, 0)	($\bar{1}$,1,0), (0,0, $\bar{1}$), (0, $\bar{2}$,0)	(0,0,0)
21	$\phi_1\phi_2\theta$	$\phi_1\phi_2\theta$	*P*2$_1$/*c*	(0, a)	(0, b)	(c, 0)	(1,1,0), (0,0,1), (1, $\bar{1}$,0)	(0,0,0)
22	$\phi_1\phi_2\theta$	$\phi_1\phi_2\bar{\theta}$	*P*$\bar{1}$	(0, a)	(0, b)	(0, c)	(1,1,0), (1, $\bar{1}$,0), (½,½,−½)	(0,0,0)
23	$\phi_1\phi_1\theta_1$	$\phi_2\phi_2\theta_2$	*P*2$_1$/*c*	(0, a)	(b, 0)	(c, d)	(0,0,1), (1, $\bar{1}$,0), (1,1,0)	(0,0,0)
24	$\phi_1$00	0$\phi_2\theta$	*C*2/*m*	(a, a)	(b, b)	(c, c)	(0,2,0), (2,0,0), (0,0, $\bar{1}$)	(0,0,0)
25	$\phi_1\phi_2\theta_1$	$\phi_3\phi_4\theta_2$	*P*$\bar{1}$	(a, b)	(c, d)	(e, f)	(1,1,0), (1, $\bar{1}$,0), (0,0, $\bar{1}$)	(0,0,0)

The symmetry analysis for in-phase ψ tilts described by the SM3 irrep, as well as those that result from the coupling of the SM3 and the X_2^+ irreps are given in Table 2. Four order parameters are needed to describe the ψ tilting, two describe rotations about the *a*- and *b*-axes in the 1st layer, and two

about the same axes in the 2nd layer. An additional five tilt systems that involve a combination of ψ-, ϕ-, and θ-tilts are given in the Supporting Information (Table S1). One interesting result from this study is that distortions involving ψ-tilts can produce noncentrosymmetric and polar space groups, whereas distortions involving only θ and ϕ tilts invariably result in centrosymmetric space groups. In retrospect, this result might have been anticipated from the fact that the X_2^+, X_3^+, and X_4^+ irreps all retain the inversion symmetry of the parent structure, hence the + superscript.

Table 2: Space group assignments and tilting schemes that arise from the SM3 irrep or a combination of SM3 and X_2^+ irreps.

#	Tilts		Space group	SM3	X_2^+	Basis	Origin
	1st layer	2nd layer					
26	0ψ0	000	*Pmma*	(a,0); (0,0)	(0, 0)	(2,0,0), (0,1,0), (0,0,1)	(0,0,0)
27	0ψ0	0$\bar{\psi}$0	*Pnma*	(a,a); (0,0)	(0, 0)	(2,0,0), (0,1,0), (0,0,1)	(¾,¼,¼)
28	ψψ0	000	*P*4/*nmm*	(a,0); (a,0)	(0, 0)	(2,0,0), (0,2,0), (0,0,1)	(0,0,0)
29	ψ00	0ψ0	*P*4$_2$/*nmc*	(0,a); (a,0)	(0, 0)	(2,0,0), (0,2,0), (0,0,1)	(−3/2,0,− ½)
30	ψψ0	$\bar{\psi}\bar{\psi}$0	*Cmce*	(a,a); (a,a)	(0, 0)	($\bar{2}$,2,0), ($\bar{2}$,$\bar{2}$,0), (0,0,1)	(−¼,7/4,¼)
31	0ψ$_1$0	0ψ$_2$0	*Pmc*2$_1$	(a,b); (0,0)	(0, 0)	(0,1,0), (0,0,1), (2,0,0)	(0,0,0)
32	ψ$_1$ψ$_2$0	000	*Pmmn*	(a,0); (b,0)	(0, 0)	(2,0,0), (0,2,0), (0,0,1)	(0,0,0)
33	ψ$_1$00	0ψ$_2$0	*Pmmn*	(0,a); (b,0)	(0, 0)	(2,0,0), (0,2,0), (0,0,1)	(−½,0,0)
34	ψ$_1$ψ$_1$0	ψ$_2$ψ$_2$0	*Abm*2	(a,b); (a,b)	(0, 0)	(0,0,$\bar{1}$), (2, $\bar{2}$,0),($\bar{2}$,$\bar{2}$,0)	(0,1,0)
35	ψ$_1$ψ$_2$θ	$\bar{\psi}_1\bar{\psi}_2\theta$	*P*2$_1$/*c*	(a,a); (b,b)	(0, c)	($\bar{2}$,0,0), (0,0,$\bar{1}$), (2,$\bar{2}$,0)	(−5/4,¾,¼)
36	ψ$_1$ψ$_2$θ	ψ$_1$ψ$_2\bar{\theta}$	*Aba*2	(a,b); (b,a)	(c, 0)	(0,0,1), ($\bar{2}$,$\bar{2}$,0), (2,$\bar{2}$,0)	(0,3/2,¼)
37	0ψ0	00θ	*Pmna*	(a,0); (0,0)	(b, b)	(0,2,0), (0,0,1), (2,0,0)	(0,0,0)
38	ψψ0	00θ	*P*4/*n*	(a,0); (a,0)	(b, b)	(0,2,0), ($\bar{2}$,0,0), (0,0,1)	(0,−1,0)
39	ψ$_1$ψ$_2$θ	000	*Pmmn*	(a,0); (b,0)	(c, −c)	(2,0,0), (0,2,0), (0,0,1)	(0,0,0)
40	ψ$_1$ψ$_2$θ	0ψ$_3$0	*Pmn*2$_1$	(a,b); (c,0)	(d, −d)	(0,2,0), (0,0,1), (2,0,0)	(0,½,0)
41	ψ$_1$ψ$_2$θ$_1$	00θ$_2$	*P*2/*c*	(a,0); (b,0)	(c, d)	($\bar{2}$,0,0), (0,0,$\bar{1}$), (2,$\bar{2}$,0)	(0,0,0)
42	ψ$_1$ψ$_2$θ$_1$	ψ$_3$ψ$_4$θ$_2$	*Pc*	(a,b); (c,d)	(e, f)	($\bar{2}$,0,0), (0,0,$\bar{1}$), (2,$\bar{2}$,0)	(0,0,0)

4. Observed patterns of octahedral tilting

The next task is to determine which patterns of octahedral tilting are most prevalent in actual compounds. To do so the Inorganic Crystal Structural Database (ICSD) and Cambridge Structural Database (CSD) were surveyed to find halide variants of the *n* = 1 Ruddlesden-Popper structure and classify their patterns of octahedral tilting. The tilt systems were determined by visual inspection of

the reported crystal structures using the VESTA3 software (Momma & Izumi, 2011), informed by the symmetry analysis discussed in the previous section.

First, the ICSD was surveyed for inorganic halide RP compounds. This resulted in 21 unique compositions (see Table S2 in the Supporting Information). The compounds containing NH_4^+ are grouped with the inorganic phases because NH_4^+ is a spherical cation with no torsional degrees of freedom, and as such behaves more like an alkali cation than an organic cation (Lanclette, *et al*., 1972). At room temperature 15 of the 21 compounds adopt the undistorted parent structure with *I*4/*mmm* symmetry. The only compounds that adopt a lower symmetry structure are those that contain a B-site cation prone to a Jahn-Teller distortion, either Cu^{2+} or Cr^{2+}. A symmetry mode analysis of cooperative Jahn-Teller distortions in K_2NiF_4 compositions shows three symmetrically distinct patterns of distortion. If the elongated axis of the octahedron is oriented perpendicular to the layers the symmetry remains *I*4/*mmm*, but if the elongated axis is located within the layers the symmetry can either be *Cmce* or *Pbam*, depending on the directions of the distortions from one layer to the next. Interestingly, these two types of cooperative Jahn-Teller distortion are equivalent by symmetry to $(00\theta)/(00\bar{\theta})$ and $(00\theta)/(00\theta)$ tilting, respectively. In all five compounds containing either Cu^{2+} or Cr^{2+}, the cooperative Jahn-Teller distortion lowers the space group symmetry to *Cmce*. While this symmetry permits $(00\theta)/(00\bar{\theta})$ tilting, an inspection of the structure shows no sign of octahedral tilting. From this, we conclude that at room temperature octahedral tilting distortions are generally not favorable in all-inorganic halides with the $n = 1$ RP structure. Low temperature structural data is available only for K_2MnF_4 and $(NH_4)_2MgF_4$. The former retains the undistorted *I*4/*mmm* structure down to 4 K, but the latter has $P2_1/c$ symmetry with the tilting scheme $(\phi_1\phi_2\theta)/(\phi_2\phi_1\bar{\theta})$ at 20 K. Note that an earlier study by Balachandran *et al*. (2014) found the undistorted *I*4/*mmm* structure is also the most common structure among oxides with the $n = 1$ RP structure.

A survey of hybrid compounds with organic cations separating the inorganic layers paints a very different picture. A search of both the CSD and ICSD revealed approximately 200 entries corresponding to layered hybrid organic-inorganic compounds with A_2BX_4 stoichiometry and either Cl^-, Br^-, or I^- as the anion. The list can be culled down to 140 unique structures by eliminating: (1) isostructural entries with the same composition, (2) entries that have *.cif files with flags that call into question their accuracy, and (3) entries where the offset between layers differs from the $a/2 + b/2$ characteristic of the RP structure. The first criterion ensures that entries originating from variable temperature studies where the same structure is observed at multiple different temperatures are counted only once. The second criterion culls out questionable structure determinations. The third criterion eliminates entries that adopt the DJ structure or a structure that is intermediate between the RP and DJ structures. This is important because if the layer shift factor differs from $a/2 + b/2$ the symmetry of the parent space group is typically altered (McNulty & Lightfoot, 2021; Alexandrov & Bartolome, 2001). Entries that were removed due to irregular layer shifts tend to be most prevalent in

compounds that have large and/or bulky organic cations. The details of the survey can be found in Tables S3 and S4 in the Supporting Information.

Table 3 summarizes the frequencies with which each tilt system is seen among hybrid layered perovskite compounds found in the CCDC and ICSD. Of the 140 unique structures, 123 (88%) adopt a structure with symmetry that matches one of the tilt systems predicted in the previous section. The reasons why some compounds have symmetries that differ from the group theory predictions ultimately comes back to structural distortions that go beyond octahedral tilting. These will be discussed in the next section.

Table 3: Frequency of tilt systems seen in A_2BX_4 hybrid halide perovskites. The entries are divided into those that have the space group symmetry predicted by group theory and those that have lower symmetry.

Tilt system	Predicted space group symmetry	Entries that agree with the prediction	Entries with symmetry lower than predicted	Total entries
No tilts				
$(000)/(000)$	$I4/mmm$	6	0	6
Only θ tilts				
$(00\theta)/(00\bar{\theta})$	$Cmce$	8	11	19
Only ϕ tilts				
$(\phi 00)/(0\phi 0)$	$P4_2/ncm$	4	0	4
$(\phi\phi 0)/(\phi\phi 0)$	$Cmce$	12	4	16
$(\phi_1\phi_2 0)/(\phi_2\phi_1 0)$	$Pccn$	3	0	3
Both θ and ϕ tilts				
$(\phi\phi\theta)/(\phi\phi\bar{\theta})$	$P2_1/c$	41	1	42
$(\phi\phi\theta)/(\phi\phi\theta)$	$Pbca$	38	1	39
$(\phi\phi\theta)/(\bar{\phi}\bar{\phi}\bar{\theta})$	$C2/c$	3	0	3
$(\phi_1\phi_2\theta)/(\phi_1\phi_2\theta)$	$P2_1/c$	1	0	1
$(\phi_1\phi_2\theta)/(\phi_1\phi_2\bar{\theta})$	$P\bar{1}$	7	0	7

The first thing to note is that unlike their all-inorganic counterparts, the undistorted structure is only seen at high temperatures (T > 340 K) and then only for six compounds. This finding is perhaps not too surprising as the point symmetry elements of the organic cations are in general not consistent with the *I*4/*mmm* symmetry of the parent structure. To realize the symmetry of the undistorted parent structure the position of the organic cation must be disordered, and dynamic motions favored at high temperatures are the most likely source of this disorder. If there were more high temperature structural

studies there might be more examples of the parent structure, though in many cases decomposition would likely occur before a temperature is reached where the *I*4/*mmm* parent structure is stabilized.

The second observation of note is that of the 47 possible tilt systems, only 9 are seen experimentally, none of which involve in-phase ψ tilts. Of those 9 tilt systems (ϕϕθ)/(ϕϕ$\bar{\theta}$) with monoclinic $P2_1/c$ symmetry and (ϕϕθ)/(ϕϕθ) with orthorhombic *Pbca* symmetry are the most common. In fact, tilt systems involving both ϕ- and θ-tilts account for ~66% of the entries. There are seven examples of ($\phi_1\phi_2\theta$)/($\phi_1\phi_2\bar{\theta}$) tilting, most of which contain large and/or bulky organic cations. It is likely that the packing of these large, often asymmetric organic cations causes the ϕ tilts within the layer to become inequivalent, lowering the space group symmetry from the monoclinic $P2_1/c$ associated with (ϕϕθ)/(ϕϕ$\bar{\theta}$) to the triclinic $P\bar{1}$ associated with ($\phi_1\phi_2\theta$)/($\phi_1\phi_2\bar{\theta}$) tilting.

Another interesting takeaway from Table 3 is the prevalence of deviations from the predicted symmetry for those compounds with (00θ)/(00$\bar{\theta}$) tilting. Over half of the entries that have only θ-tilts possess a space group symmetry lower than *Cmce*, in most cases the polar $Cmc2_1$ space group. As discussed in the next section, this symmetry lowering is caused by a combination of orientational ordering of the organic cations and distortions of the octahedra.

Figure 4 shows that the types of tilts present depend in part on the composition of the inorganic layer. Examples of (00θ)/(00$\bar{\theta}$) tilting are found predominantly in compounds where the inorganic cation is either Pb^{2+} or Sn^{2+}, both of which are prone to stereoactive lone pair distortions. In contrast, examples where only ϕ-tilts are seen almost exclusively in compounds containing smaller inorganic cations such as Mn^{2+}, Fe^{2+}, and Cd^{2+} paired with the smaller chloride ion. The third group of compounds are those containing Cu^{2+} where a pronounced Jahn-Teller distortion leads to an ordered pattern of long and short bridging Cu–X bonds within the inorganic layers. As noted earlier, the cooperative Jahn-Teller distortion has symmetry consequences that are identical to θ-tilting. Consequently, the combination of a cooperative Jahn-Teller distortion and ϕ-tilting would look very much like the combination of ϕ- and θ-tilting. Visual inspection of A_2CuX_4 structures shows that in some cases θ-tilts are clearly present, while in other cases they so small that they could be ignored. Once the effects of the cooperative Jahn-Teller distortion are considered the patterns of octahedral tilting seen in A_2CuX_4 compositions are similar to those compounds containing Mn^{2+}, Fe^{2+}, and Cd^{2+}.

It's also important to recognize that many compounds undergo changes in tilt system as a function of temperature. As such, temperature becomes an important variable when assessing the stabilities of competing tilt systems. Among compositions that contain divalent manganese, iron, or cadmium it is common to see both ϕ- and θ-tilts at low temperatures, but as the temperature increases the θ-tilts are lost (i.e. they become dynamic) leaving only ϕ-tilts.

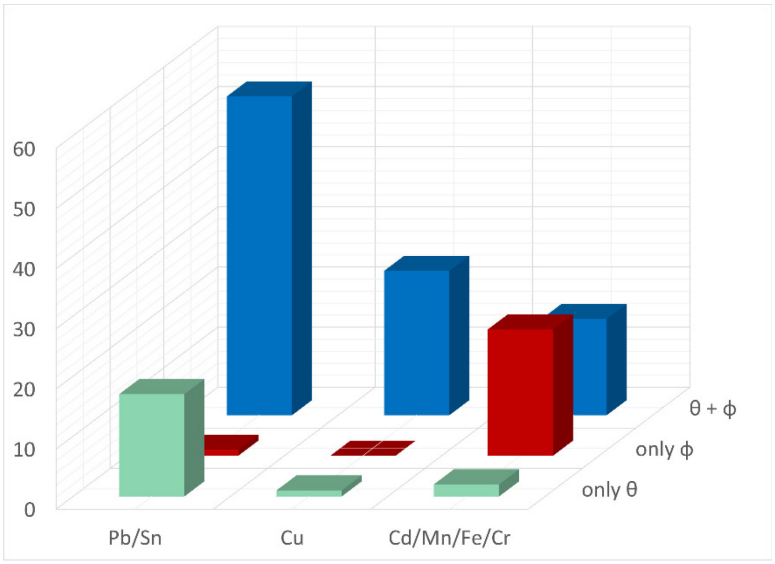

Figure 4: The prevalence of ϕ- and θ-tilts as a function of the identity of the inorganic cation.

5. Understanding tilt system preferences

The analysis given in the previous section raises several questions. Why are some tilt systems favored over others? Why aren't ψ-tilts observed? How do the identity and attributes of the inorganic cation, the halide ion, or the organic cation affect the stabilities of competing tilt systems? What types of distortions are responsible for further reduction in symmetry and under what circumstances might we expect to observe them?

The structure directing forces that are operative in hybrid n = 1 RP phases include polar-covalent bonding within the inorganic layers, noncovalent interactions (mostly dispersion forces) between organic cations, and hydrogen bonding between the organic cations and inorganic layers. The lack of octahedral tilting distortions in all-inorganic n = 1 RP phases suggests that bonding interactions within the inorganic layers are not the driving force behind octahedral tilting. Any impact of octahedral tilting on the packing of the organic cations would be a second order effect. Therefore, we can assume that octahedral tilting distortions are largely driven by hydrogen bonding interactions between the ammonium head groups of the organic cations and the halide ions of the inorganic layer.

In the undistorted parent structure, the A-site cation sits on a site with 4*mm* (C_{4v}) symmetry. It is surrounded by four terminal halide ions and four bridging halide ions. The presence of eight halide ions around the $-NH_3^+$ head group of the organic cation is not optimal for forming strong hydrogen bonds. Octahedral tilting distortions lower the symmetry, allowing some halide ions to move toward the ammonium head group while others move away. Tilt systems that create an environment where each hydrogen on the $-NH_3^+$ can form a strong hydrogen bond with a single halide ion will presumably be the most favorable.

Figure 5 shows the movements of the halide ions resulting from either ψ-, ϕ-, or θ-tilts within a single layer. The first thing to note is that ψ-tilting creates two chemically inequivalent sites for the organic cations. For the sites shaded in blue, two of the four bridging halides move upward toward the A-site cation and all four terminal halides move away from the A-site cation. For the sites shaded in pink, the halide ions move in the opposite sense. Thus, we see that ψ-tilts create inequivalent environments for the organic cations, a violation of Pauling's rule of parsimony (Pauling, 1929), which helps to explain why ψ-tilts are so rare.

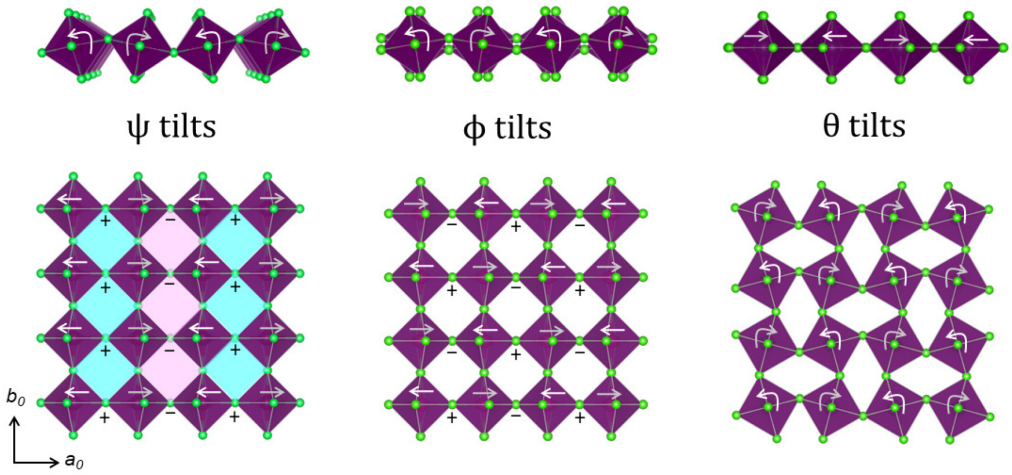

Figure 5: The halide ion displacements within a single BX_4^{2-} layer with a ψ-tilt (left), a ϕ-tilt (center), or a θ-tilt (right), as viewed parallel (top) and perpendicular (bottom) to the layer. The + and – symbols indicate the movement of the bridging halide ions above and below the plane of the projection, respectively. The blue and pink shading shown in the lower left diagram highlights the chemical inequivalence of the A-sites resulting from ψ-tilts.

The chemical and crystallographic inequivalence of the A-sites is not just for tilt systems with a (ψ00) layer. It is common to all tilt systems with in-phase ψ-tilts. Figure 2d shows that this effect is even more pronounced for a layer with (ψψ0) tilting. A similar feature is known for three-dimensional perovskites, where in-phase tilts about two or more axes lead to chemically inequivalent A-sites. In 3D perovskites, these patterns of tilting can generally only be stabilized by using A-site cations of different sizes and bonding preferences (Woodward, 1997b). One such example is $CaCu_3Ti_4O_{12}$, where (ψψψ) tilting preserves the 12-fold coordination of the Ca^{2+} ion while the smaller Cu^{2+} ion adopts a 4-fold square planar coordination environment (Subramanian, et al., 2000). It is not out of the question that a judicious choice of two or more organic cations might be used to a similar effect in layered hybrid perovskites. In fact, in-phase tilts are observed in two compositions containing a 1:1 mixture of different A-site cations— (methylammonium, guanidinium)PbI_4 and (cesium,

guanidinium)$PbBr_4$—albeit with a ½ *a* + 0 *b* layer shift that is intermediate between an RP and a DJ phase (McNulty & Lightfoot, 2021).

Next, we turn our attention to tilt systems containing ϕ- and/or θ-tilts. The temperature dependent structural evolution of $(CH_3NH_3)_2CdCl_4$ is illustrative. Not only does the small size of the methylammonium cation minimize dispersion forces within the organic layer, but this compound also adopts three different tilt systems as a function of temperature: (ϕϕθ)/(ϕϕθ̄) at 100 K, (ϕ00)/(0ϕ0) at 234 K, and (ϕϕ0)/(ϕϕ0) at 295 K (Chapuis, et al., 1975). The hydrogen bonding interactions in each of these tilt systems are shown in Figure 6. As the temperature is lowered and the effects of entropy are reduced, the enthalpy term, which contains a contribution from hydrogen bonding, makes an ever-larger contribution to the free energy. From this we can infer that the strength of the hydrogen bonding increases as the temperature is lowered: (ϕϕ0)/(ϕϕ0) < (ϕ00)/(0ϕ0) < (ϕϕθ)/(ϕϕθ̄). At first glance, this relative order is not obvious, as the H−Cl distances are on average shortest at room temperature where (ϕϕ0)/(ϕϕ0) tilting is observed.

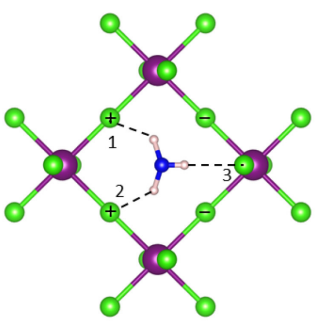

(ϕϕ0)/(ϕϕ0)
Cmce
T = 295 K

H-bond	H-Cl dist	N-H-Cl ∠
1	2.42 Å	138°
2	2.42 Å	138°
3	2.38 Å	164°

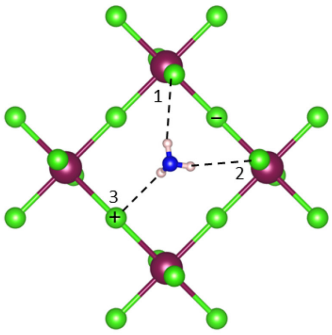

(ϕ00)/(0ϕ0)
P4_2/*ncm*
T = 234 K

H-bond	H-Cl dist	N-H-Cl ∠
1	2.59 Å	155°
2	2.59 Å	155°
3	2.57 Å	147°

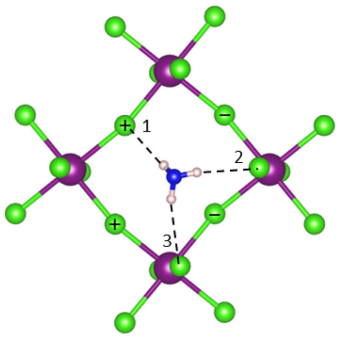

(ϕϕθ)/(ϕϕθ̄)
P2_1/*c*
T = 100 K

H-bond	H-Cl dist	N-H-Cl ∠
1	2.44 Å	167°
2	2.36 Å	165°
3	2.56 Å	152°

Figure 6: Hydrogen bonding in $(CH_3NH_3)_2CdCl_4$ at three different temperatures. The dashed lines represent the closest halide ion to each hydrogen of the $-NH_3^+$ head group. The + and – symbols indicate movements of the bridging chloride ions either above (+) or below (−) the plane of the image. The $CH_3NH_3^+$ cation shown is located above the $CdCl_4^{2-}$ layer.

To better understand this order of the phase transitions in $(CH_3NH_3)_2CdCl_4$ we need to consider the hydrogen bonding interactions more carefully. Let's begin by putting the H−Cl distances and N−H−Cl angles into context. Steiner reviewed the distribution of hydrogen bond distances and angles in halide

salts of various organic cations, including primary ammonium cations (Steiner, 1998). He found that for "nearly linear" hydrogen bonds, defined as those with N−H−Cl angles >140°, the average H−Cl distance was 2.247(5) Å and nearly all of these bonds fell between 2.1 and 2.5 Å. In layered hybrid perovskites, the hydrogen bonds are on the longer side of this distribution because the chlorides form either one or two covalent bonds with cadmium and therefore have less bonding capacity than a free halide ion. However, based on Steiner's distance criterion we could qualitatively assign three strong hydrogen bonds in (ϕϕ0)/(ϕϕ0), three weak hydrogen bonds in (ϕ00)/(0ϕ0), and two strong plus one weak hydrogen bond in (ϕϕθ)/(ϕϕ$\bar{\theta}$). Although this analysis neglects the N−H−Cl angles, which are closer to linear in (ϕϕθ)/(ϕϕ$\bar{\theta}$) than they are in the other two tilt systems.

Next, we consider the bonding requirements of the chloride ions. In a simplistic model where the Cd−Cl bonds are all treated as equivalent, the +2 oxidation state of cadmium dictates a valence of 2/6 = 1/3 for each Cd−Cl bond. Therefore, the bridging halide ion gets 2×(1/3) = 2/3, and the terminal halide ion gets 1×(1/3) = 1/3 of its expected valence from bonding to cadmium. The unfulfilled bonding must come from hydrogen bonds. In practice, the terminal Cd−Cl bonds are somewhat shorter (2.537(4) Å) than the terminal Cd−Cl bonds (2.644(3) Å) at 295 K, but that does not invalidate the notion that the terminal chlorides must form either stronger or more numerous hydrogen bonds than the bridging chlorides.

We can be more quantitative if we calculate bond valence sums from the experimentally observed Cd−Cl bond distances (Brown, 2016). If we neglect any contribution from hydrogen bonds, the bond valence sum at the terminal chloride ion is 0.44, while the bond valence sum of the bridging chloride ion is 0.65. Similar bond valence sums are obtained for a series of Pb-containing n = 1 hybrid RP phases (see Figure S3 in the Supporting Information), where the terminal halides are found to have bond valence sums ranging from 0.36 to 0.44, and the bridging halides values ranging from 0.71 to 0.85.

Returning to Figure 6, notice that (ϕϕ0)/(ϕϕ0) tilting leads to one hydrogen bond with a terminal halide and two with bridging halides. It follows that in this structure each terminal halide forms one hydrogen bond, while each bridging halide forms two hydrogen bonds. This configuration, referred to as the bridging configuration by Mitzi (2007), is at odds with the bonding requirements of the halide ions within the inorganic layer. In contrast, the patterns of hydrogen bonding seen in (ϕ00)/(0ϕ0) and (ϕϕθ)/(ϕϕ$\bar{\theta}$) have the opposite configuration, two bonds to terminal halides and one to a bridging chloride. This configuration, dubbed the terminal configuration, is better able to meet the bonding requirements of the chloride ions in the inorganic layer, which may help to explain why these tilt systems are more stable. Of the two, (ϕϕθ)/(ϕϕ$\bar{\theta}$) has hydrogen bonds that are both shorter and closer to the ideal linear geometry. This allows us to rationalize why the hydrogen bonding seen in (ϕϕθ)/(ϕϕ$\bar{\theta}$) is more favorable than realized in the other two tilt systems.

Of the tilt systems seen in real compounds only (ϕϕ0)/(ϕϕ0) leads to the less favorable bridging configuration. Yet there are no less than seven different A_2CdX_4 compositions that have (ϕϕ0)/(ϕϕ0) tilting. Examples are found for *n* =1 RP phases with iron and manganese as well. However, in those cases where diffraction studies have been carried out at low temperatures, the (ϕϕ0)/(ϕϕ0) pattern usually transforms to a tilt system with both ϕ- and θ-tilting upon cooling. It should also be noted that for organic cations larger than methylammonium ($CH_3NH_3^+$) the symmetry elements associated with (ϕϕ0)/(ϕϕ0) tilting lead to disorder in the positions of the hydrocarbon part of the organic cation. Presumably, the configurations and/or orientations of the organic cation are dynamic at high temperatures and couple to dynamic θ-tilts of the inorganic layer. At low temperatures, these lattice vibrations freeze out leading to a transition into a tilt system with both ϕ- and θ-tilts.

Finally, let's consider the competition between the two most common tilt systems: (ϕϕθ)/(ϕϕ$\bar{\theta}$) which leads to monoclinic $P2_1/c$ symmetry and (ϕϕθ)/(ϕϕθ) which leads to orthorhombic *Pbca* symmetry. Because the tilting in any one layer is of the (ϕϕθ) type in both tilt systems, very similar patterns of hydrogen bonding emerge. However, the alternation in the direction of the θ-tilts seen in the *Pbca* structure will lead to slightly different orientations of the organic cations than those seen in the $P2_1/c$ structure. This suggests that dispersion forces between organic cations play a key role in the competition between these two tilt systems. Evidence to support this hypothesis can be found among the behavior of *n* = 1 lead iodide RP phases containing linear alkyl ammonium cations, $(H(CH_2)_nNH_3)_2PbI_4$ (Billing & Lemmerer, 2007, 2008; Lemmerer & Billing, 2012). For compounds with n ≤ 10, a transition from (ϕϕθ)/(ϕϕ$\bar{\theta}$) tilting to (ϕϕθ)/(ϕϕθ) tilting occurs upon heating. In contrast, those compositions with even longer alkyl ammonium cations (n = 12, 14, 16, and 18) show the opposite behavior, (ϕϕθ)/(ϕϕθ) is more stable at low temperatures and (ϕϕθ)/(ϕϕ$\bar{\theta}$) at high temperatures. The alkylammonium copper chloride series, $(H(CH_2)_nNH_3)_2CuCl_4$, also shows an interesting dependence on the length of the organic cation. At room temperature (ϕϕθ)/(ϕϕ$\bar{\theta}$) tilting and monoclinic symmetry are seen when the organic cation is methylammonium, whereas (ϕϕθ)/(ϕϕθ) tilting and orthorhombic symmetry is observed for ethylammonium copper chloride.

6. Distortions other than octahedral tilting

The relative abundance of hybrid *n* = 1 RP phases with (00θ)/(00$\bar{\theta}$) tilting seen in Table 3 is somewhat surprising. As we can see from Figure 5 the positions of the terminal halide ions are not affected much by θ-tilting and remain equidistant from the center of the cavity where the $-NH_3^+$ group sits. In this geometry how can strong hydrogen bonds to the terminal halides form, as needed to satisfy their bonding requirements? A closer look at the entries in the Supporting Information (Tables S3 and S5) shows that many compositions with (00θ)/(00$\bar{\theta}$) tilting undergo a transition from *Cmce* to $Cmc2_1$ on cooling. The crystal structures of one such example, $(BzA)_2PbCl_4$ (BzA = benzylammonium, $C_6H_5CH_2NH_3^+$), are shown at temperatures above and below this phase transition

in Figure 7 (Liao, et al., 2015). On the left-hand side, we see the structure at 453 K in the high temperature *Cmce* symmetry. The absence of ϕ-tilts and the presence of large θ-tilts can clearly be seen, along with the disorder of the BzA cations. Ignoring the disorder, the shortest H−Cl distance is 2.59 Å and the shortest distance between a hydrogen and a terminal chloride is 2.68 Å. In the low temperature $Cmc2_1$ structure, the BzA cations adopt an ordered pattern and the terminal chloride ions shift toward two of the four neighboring $-NH_3^+$ groups. This leads to a pattern of strong hydrogen bonds with H−Cl distances of 2.33 to 2.35 Å and N−H−Cl angles ranging from 163° to 172° shown in Figure 7e. These hydrogen bonds are comparable in strength to the strongest bonds seen in the low temperature structure of $(CH_3NH_3)_2CdCl_4$ discussed above. The third hydrogen atom on the ammonium head group is equidistant between the two bridging chloride ions, forming a weaker bifurcated hydrogen bond with an H−Cl distance of 2.63 Å to both bridging chlorides.

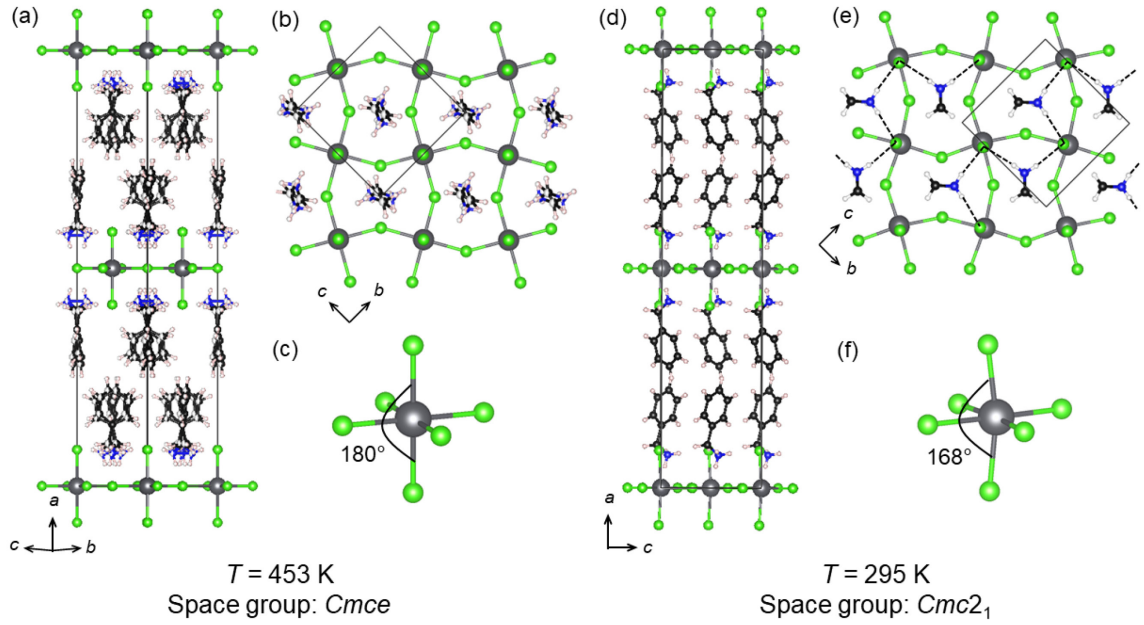

Figure 7: The crystal structures of $(C_6H_5CH_2NH_3)_2PbCl_4$ at 453 K (left) and 295 K (right). Views of the high temperature centrosymmetric structure include (a) the unit cell as viewed parallel to the inorganic layers, (b) a top-down view of a single inorganic layer, where the benzyl groups of the organic cation are not shown for clarity, and (c) the Pb-centered octahedron. Comparable views of the low temperature polar structure are shown in parts (d), (e), and (f), with strong hydrogen bonds denoted by dashed lines in (d). The axes shown in parts (a) and (d) refer to the standard setting of these two space groups.

Interestingly the terminal chloride ions above and below each Pb^{2+} ion shift in the same direction, which destroys the inversion center present in the high temperature structure and bends the Cl−Pb−Cl bond angle from the linear 180° seen in the high temperature structure to 168° (Figures 7c and 7f). As can be seen in Figure 7e half of the positively charged $-NH_3^+$ groups are pointing parallel to $[0\bar{1}1]$

and the other half parallel to [011]. When combined the net result is a permanent dipole moment along the *c*-axis, which is the polar axis for the *Cmc*2$_1$ space group. $(BzA)_2PbCl_4$ not only adopts a polar structure below 436 K, the polar axis can be reversed with an electric field making it a ferroelectric. It's notable that nearly all hybrid n = 1 RP phases that show this phase transition contain either Pb^{2+} or Sn^{2+}. The $5s^2/6s^2$ electron configuration of these ions may play a role in stabilizing the deformations of the octahedra that accompany the orientational ordering of the organic cations. A subtle distortion is also seen in the pattern of bonds in the plane defined by lead and the bridging chloride ions, with two Pb−Cl bond distances of 2.84 Å and two distances of 2.89 Å in the low temperature *Cmc*2$_1$ structure. However, this type of distortion is also seen in Cd-containing RP phases with benzylammonium and cyclohexylammonium cations, so the attributes of the organic cation appear to also play a role.

Symmetry lowering due to orientational ordering of the organic cations is not exclusive to compounds containing Pb^{2+} or Sn^{2+} and (00θ)/(00$\bar{\theta}$) tilting (see Table S5 in the Supporting Information). Both $(IBA)_2CdBr_4$ (IBA = isobutylammonium, $(CH_3)_2CH_2CH_2NH_3^+$) and $(IPA)_2CdCl_4$ (IPA = isopropylammonium, $(CH_3)_2CH_2CH_2CH_2NH_3^+$) have room temperature structures with (ϕϕ0)/(ϕϕ0) tilting and *Cmce* symmetry. In both compounds, a transition into the polar space group *C*2*ce* (or non-standard setting *Aea*2) driven by the orientational ordering of the organic cations occurs upon cooling.

Up to this point, we have largely focused on distortions of the inorganic layers and how those distortions impact hydrogen bonding, but the identity and attributes of the organic cation and the halide anion also play a role in determining the relative stability of competing structural distortions. The $(BzA)_2PbCl_4$ structure discussed above undergoes a *Cmce* to *Cmc*2$_1$ phase transition at ~436 K (Liao, et al, 2015). At room temperature $(BzA)_2PbBr_4$ also possesses *Cmc*2$_1$ symmetry (Du, et al., 2017), whereas $(BzA)_2PbI_4$ adopts a structure with (ϕϕθ)/(ϕϕ$\bar{\theta}$) tilting and *Pbca* symmetry at room temperature (Papavassiliou, et al., 1999). This suggests that the distortion that stabilizes the *Cmc*2$_1$ structure becomes less favorable as the halide ion becomes larger and less electronegative. The prevalence of (00θ)/(00$\bar{\theta}$) tilting among A_2PbX_4 and A_2SnX_4 compositions seems to be limited primarily to compositions containing aromatic or cyclic ammonium cations, while those containing linear alkyl ammonium cations tend to exhibit tilt systems with both ϕ- and θ-tilts. From this observation, one can infer that the packing of the organic cations plays a role in determining the competition between (00θ)/(00$\bar{\theta}$) tilting and (00θ)/(00$\bar{\theta}$) tilting.

7. Conclusions

Using ISODISTORT the symmetry consequences of octahedral tilting in hybrid layered perovskites with the n = 1 RP structure have been analyzed. Twenty-five different patterns of octahedral tilting are obtained by combining tilts/rotations about the *c*-axis (θ-tilts) of the *I*4/*mmm* parent structure and out-of-phase tilts about the *a*- and *b*-axes of the parent structure (ϕ-tilts). An additional twenty-two

patterns of tilting are obtained when in-phase tilts (ψ-tilts) about the *a*- and *b*-axes are considered. The predicted structures have been compared with the structures of hybrid halide perovskites found in the CSD and ICSD. Of the 140 unique structures found in these databases 123 (88%) adopt structures that are consistent with the predictions of the symmetry analysis. Of the 47 possible tilt systems, only 9 are seen experimentally (excluding the undistorted parent structure), none of which involve ψ tilts. In contrast, distortions involving both ϕ- and θ-tilts are common, accounting for ~66% of the entries. The combination of ϕ- and θ-tilts is stabilized by favorable hydrogen bonding interactions between the organic cations and the inorganic layers. For the remaining 12% of the structures, the symmetry is further lowered by effects such as orientational ordering of the organic cations and/or distortions of the octahedra. Distortions that go beyond octahedral tilting are particularly prominent in compounds with $(00\theta)/(00\bar{\theta})$ tilting that contain either Pb^{2+} or Sn^{2+} ions. In those compounds, distortions of the octahedra offer an alternate route to the formation of strong hydrogen bonding interactions.

References

Aleksandrov, K. S. (1987). *Kristallografiya*, **32**, 937.

Aleksandrov, K. S. & Bartolome, J. (2001). *Phase Transitions* **74**, 255–335.

Aleksandrov, K. S. & Bartolome, J. (1994). *J. Phys. Condens. Matter* **6**, 8219–8235.

Aleksandrov, K. S., Beznosikov, B. V., Misyul, S. V. (1987a). *Phys. Status Solidi*, **104**, 529–543.

Aleksandrov, K. S., Beznosikov, B. V., Misyul S. V. (1987b). *Ferroelectrics*, **73**, 201–220.

Asensio, Y., Marras, S., Spirito, D., Gobbi, M., Ipatov, M., Casanova, F., Mateo-Alonso, A., Hueso, L. E., Martin-Garcia, B. (2022). *Adv. Funct. Mater*. 2207988.

Attfield, J. P. (1998). *Chem. Mater*. **10**, 3239–3248.

Baikie, T., Fang, Y. N., Kadro, J. M., Schreyer, M., Wei, F. X., Mhaisalkar, S. G., Graetzel, M., White, T. J. (2013). *J. Mater. Chem. A*, **1**, 5628–2641.

Balachandran, P. V., Puggioni, D., Rondinelli, J. M. (2014). *Inorg. Chem*. **53**, 336–348.

Billing, D. G. & Lemmerer, A. (2007). *Acta Cryst*. B**63**, 735–747.

Billing, D. G. & Lemmerer, A. (2008). *New J. Chem*. **32**, 1736.

Brown, I.D. (2016). The chemical bond in inorganic chemistry: The bond valence model, 2nd edn. Oxford University Press, Oxford.

Campbell, B. J., Stokes, H. T., Tanner, D. E. & Hatch, D. M. (2006). *J. Appl. Cryst*. **39**, 607–614.

Chapuis, G., Arend, H., Kind R. (1975). *Physica Status Solidi A*, **31**, 449–454.

Du, K. Z., Tu, Q., Zhang, X., Han, Q. W., Liu, J., Zauscher, S., Mitzi, D. B. (2017). *Inorg. Chem*. **56**, 9291–9302.

Frost, J. M., Butler, K. T., Brivio, F., Hendon, C. H., van Schilfgaarde, M., Walsh, A. (2014). *Nano Lett*. **14**, 2584–2590.

Glazer, A. M. (1972). *Acta Cryst*. B**63**, 3384–3392.

Gray, M. B., Majher, J. D., Strom, T. A., Woodward, P. M. (2019). *Inorg. Chem*. **58**, 13403–13410.

Hatch, D. M., Stokes, H. T., Aleksandrov, K. S., Misyul, S. V. (1989). *Phys. Rev. B*, **39**, 9282–9288.

Howard, C. J. & Stokes, H. T. (1998). *Acta Cryst*. B**54**, 782–789.

Howard, C. J., Kennedy, B. J., Woodward, P. M. (2003). *Acta Cryst*. B**59**, 463–471.

Hwang, H. Y., Cheong, S. W., Radaelli, P. G., Marezio, M., Batlogg, B. (1995). *Phys. Rev. Lett*. **75**, 914–917.

Lalancette, R. A., Elliott, N., Bernal, I. (1972). *J. Cryst. Mol. Struct*., **2**, 143–149.

Lemmerer, A. & Billing, D. G. (2012). *Dalt. Trans*. **41**, 1146–1157.

Li, J. N., Barrio, M., Dunstan, D. J., Dixey, R., Lou, X. J., Tamarit, J. L., Phillips, A. E., Lloveras, P. (2021). *Adv. Funct. Mater*. **31**, 2105154.

Liao, W. Q., Zhang, Y., Hu, C. L., Mao, J. G., Ye, H. Y., Li, P. F., Huang, S. P. D., Xiong, R. G. (2015). *Nat. Commun*. **6**, 7338.

Lin, K. B., Xing, J., Quan, L. N., de Arquer, F. P. G., Gong, X. W., Lu, J. X., Xie, L. Q., Zhao, W. J., Zhang, D. Yan, C. Z., Li, W. Q., Liu, X. Y., Lu, Y. Kirman, J., Sargent, E. H., Xiong, Q. H., Wei, Z. H. (2018). *Nature*, **562**, 245–248.

Linaburg, M. R., McClure, E. T., Majher, J. D., Woodward, P. M. (2017). *Chem. Mater*. **29**, 3507–3514.

Majher, J. D., Gray, M. B., Strom, T. A., Woodward, P. M. (2019). *Chem. Mater*. **31**, 1738–1744.

Mahesh, R., Mahendiran, R., Raychaudhuri, A. K., Rao, C. N. R. (1995). *J. Solid State Chem*. **120**, 204–207.

McNulty, J. A., Lightfoot, P. (2021). *IUCrJ* **8**, 485–513.

Miller, S. C. & Love, W. F. (1967). Tables of Irreducible Representations of Space Groups and Co-representations of Magnetic Space Groups. Boulder: Pruett.

Mitzi, D.B. (2007). Synthesis, Structure, and Properties of Organic Inorganic Perovskites and Related Materials. In: Progress in Inorganic Chemistry, John Wiley & Sons, Inc., Hoboken, 1–121.

Momma, K. & Izumi, F (2011). *J. Appl. Crystallogr*. **44**, 1272–1276.

Papavassiliou, G. C., Mousdis, G. A., Raptopoulou, C., Terzis, A. (1999). *Z. Naturforsch. B* **54**, 1405–1409.

Pauling, L. (1929). *J. Am. Chem. Soc*. **51**, 1010–1026.

Seo, J., McGillicuddy, R. D., Slavney, A. H., Zhang, S., Ukani, R., Yakovenko, A. A., Zheng, S. L., Mason, J. A. (2022). *Nat. Commun*. **13**, 2536.

Steiner, T. (1998). *Acta Cryst*. B**54**, 456−463, (1998).

Stokes, H. T., Kisi, E. H., Hatch, D. M., Howard, C. J. (2002). *Acta Cryst*. B**58**, 934–938.

Stoumpos, C. C., Malliakas, C. D., Kanatzidis, M. G. (2013). *Inorg. Chem*. **52**, 9019–9038.

Stranks, S. D., Eperon, G. E., Grancini, G., Menelaou, C., Alcocer, M. J. P., Leijtens, T., Herz, L. M., Petrozza, A., Snaith, H. J. (2013). *Science*, **342**, 341–344.

Subramanian, M. A., Li, D., Duan, N., Reisner, B. A., Sleight, A. W. (2000). *J. Solid State Chem*. **151**, 323–325.

Woodward, P. M. (1997a). *Acta Cryst*. B**53**, 32–43.

Woodward, P. M. (1997b). *Acta Cryst*. B**53**, 44–66.

Yeh, S. K., Wu, S. Y., Lee, C. S., Wang, Y. (1993). *Acta Cryst*. **B**49, 806–811.